Dalton Transactions

ROYAL SOCIETY OF CHEMISTRY

PAPER

View Article Online
View Journal | View Issue



Cite this: *Dalton Trans.*, 2024, **53**, 10486

# Adsorption properties of M-UiO-66 (M = Zr(IV); Hf(IV) or Ce(IV)) with BDC or PDC linker†

Diego González,[a] Cesar Pazo-Carballo, *[a,b,d] Esteban Camú, [c,d] Yoan Hidalgo-Rosa,[d,f] Ximena Zarate,[e] Néstor Escalona [b,c,d] and Eduardo Schott *[a,d]

The increasing $CO_2$ emissions and their direct impact on climate change due to the greenhouse effect are environmental issues that must be solved as soon as possible. Metal–organic frameworks (MOFs) are one class of crystalline adsorbent materials that are thought to have enormous potential in $CO_2$ capture applications. In this research, the effect of changing the metal center between Zr(IV), Ce(IV), and Hf(IV), and the linker between BDC and PDC has been fully studied. Thus, the six UiO-66 isoreticular derivatives have been synthesized and characterized by FTIR, PXRD, TGA, and $N_2$ adsorption. We also report the BET surface area, $CO_2$ adsorption capacities, kinetics, and the adsorption isosteric heat ($Q_{st}$) of the UiO-66 derivatives mentioned family. The $CO_2$ adsorption kinetics were evaluated using pseudo-first order, pseudo-second order, Avrami's kinetic models, and the rate-limiting step with Boyd's film diffusion, interparticle diffusion, and intraparticle diffusion models. The isosteric heats of $CO_2$ adsorption using various MOFs are in the range 20–65 kJ mol$^{-1}$ observing differences in adsorption capacities between 1.15 and 4.72 mmol g$^{-1}$ at different temperatures due to the electrostatic interactions between $CO_2$ and extra-framework metal ions. The isosteric heat of adsorption calculation in this report, which accounts for the unexpectedly high heat released from Zr-UiO-66-PDC, is finally represented as an increase in the interaction of $CO_2$ with the PDC linker and an increase in $Q_{st}$ with defects.

Received 30th March 2024,
Accepted 27th May 2024

DOI: 10.1039/d4dt00941j

rsc.li/dalton



## 1. Introduction

The increasing $CO_2$ concentration in the atmosphere and its direct impact on climate change due to the greenhouse effect is an environmental issue that needs to be solved as soon as possible. The $CO_2$ storage technologies (which would decrease the atmospheric $CO_2$ concentration) have the risk of causing other challenges like energy waste and cost.[1–3] To store $CO_2$ physisorption on high surface area compounds could be a more efficient option, being less energetic than other processes and the smaller amount of adsorbent needed, due to the increased surface area of those materials.

Various $CO_2$ adsorbents[4] with large surface areas like activated carbon,[5,6] zeolites,[7,8] mesoporous silica,[3,9] and molecular sieves,[10] have been investigated. Metal–organic frameworks (MOFs) have recently been presented as a new viable $CO_2$ adsorbent option.[4] These materials have porous crystalline structures composed by a metal cluster (or node) linked with a polydentate organic compound (linker). MOFs have many favorable functional characteristics for adsorption, including a tunable structure with adaptable pore size, high surface areas, and crystallinity, the possibility of adding functional groups by post-synthetic modifications, and high adsorption capacities, among others.[11–13] These characteristics are used for applications like catalysis, drug delivery, sensing, and gas storage/separation.[12]

$CO_2$ adsorption has been explored for several different MOFs, including CU-BTC, ZIF-8, BIO-MOF-1, MIL-101, UiO-66, among others.[4,11,14,15] Of our interest is UiO-66, which is a MOF with an octahedral metal cluster with a molecular

[a]*Departamento de Química Inorgánica, Facultad de Química y Farmacia, Centro de Energía UC, Centro de Investigación en Nanotecnología y Materiales Avanzados CIEN-UC, Pontificia Universidad Católica de Chile, Avenida Vicuña Mackenna, 4860, Santiago, Chile. E-mail: edschott@uc.cl*
[b]*Departamento de Química Física, Facultad de Química y Farmacia, Pontificia Universidad Católica de Chile, Avenida Vicuña Mackenna 4860, Santiago, Chile*
[c]*Departamento de Ingeniería Química y Bioprocesos, Escuela de Ingeniería, Pontificia Universidad Católica de Chile, Avenida Vicuña Mackenna 4860, Macul, Santiago, Chile*
[d]*Millennium Nuclei on Catalytic Processes towards Sustainable Chemistry (CSC), Chile*
[e]*Instituto de Ciencias Aplicadas, Theoretical and Computational Chemistry Center, Facultad de Ingeniería, Universidad Autónoma de Chile, Av. Pedro de Valdivia 425, Santiago, Chile*
[f]*Centro de Nanotecnología Aplicada, Facultad de Ciencias, Ingeniería y Tecnología, Universidad Mayor, Camino La Pirámide 5750, Huechuraba, Santiago, Chile*

†Electronic supplementary information (ESI) available. See DOI: https://doi.org/10.1039/d4dt00941j

formula $M_6O_4(OH)_4$, originally prepared with M = Zr(IV).[16] However, UiO-66 can also be synthesized using other metals, such as Ce(IV), Hf(IV), and Th(IV), generating an isoreticular metal cluster.[17] These metallic clusters are interconnected by terephthalic acid linkers (BDC), creating a fcu topology. Furthermore, the linker can be modified by adding functional groups (FG)[18] such as $-NH_2$, $-OH$, $-NO_2$, $-Br$, $-OMe$, $-CH_3$, $-CO_2H$, $-SO_3H$, $-CF_3$ to the aromatic ring by means of post-synthetic modifications[19,20] or using the functionalized BDC linker in the synthetical procedure of UiO-66-(FG).[13,20–23] Also, the linker can be substituted with 2,5-pirydinedicarboxilic acid (PDC) on the direct synthesis.[24] Isoreticular MOFs with UiO-66 typology have three different pore sizes in the micropore region, one octahedral pore (~11 Å), a tetrahedral pore (~8 Å), and a window pore that connect both cavities (~6 Å). Those micropores allow the material to reach a surface area of over 1200 $m^2\ g^{-1}$.[25,26] Thus, UiO-66 and its isoreticular derivatives exhibit a critical set of characteristics that allow for ambient $CO_2$ adsorption. UiO-66 is the material with the most appealing physicochemical features for $CO_2$ capture due to its remarkable water resistance and great thermal, chemical, mechanical, and pH stability.[16,22,24] Thus, industrial treatments and atmospheric environment are not a challenge for UiO-66.

It has been observed that the UiO-66 functionalization enhances the adsorption capacities of the material,[13] particularly, UiO-66-$NH_2$ has shown theoretically[18] and experimentally[19,22,27,28] one of the best results for $CO_2$ adsorption and selectivity. Also, the change of the metal center produces differences in the $CO_2$ adsorption capacities.[29–31] To use PDC linker is of particular interest due to the nitrogen free electron pair presence, which would show a behavior than the amino group in UiO-66-$NH_2$. Therefore, the $CO_2$ adsorption capabilities for UiO-66 with linkers (BDC and PDC) combined with metal centers M = Zr(IV), Ce(IV), and Hf(IV) were investigated in this report.

Although the adsorption of a maximum amount of $CO_2$ is important, knowing the kinetics of the process and the study of the $CO_2$ adsorption heat (isosteric heat) is also of great importance to search applications such as $CO_2$ concentration. Thus, the final goal would be to generate a mitigation methodology to obtain a sustainable process that improves the current methods of $CO_2$ concentration.

In the herein report, it is fully studied and discusses the effect of changing the metal center between Zr(IV), Ce(IV), and Hf(IV), and the linker between BDC and PDC. Thus, the six UiO-66 isoreticular derivatives have been synthesized and characterized by FTIR, PXRD, TGA, and $N_2$ adsorption. We also report the BET surface area, $CO_2$ adsorption capacities, kinetics, and the adsorption isosteric heat ($Q_{st}$) of the UiO-66 derivatives mentioned family. The $CO_2$ adsorption kinetics were evaluated using pseudo-first order, pseudo-second order, Avrami's kinetic models, and the rate-limiting step with Boyd's film diffusion, interparticle diffusion, and intraparticle diffusion models. The isosteric heat of $CO_2$ adsorption was calculated using the Clausius–Clapeyron equation. Furthermore, DFT calculations over the whole family of derivatives were performed to explain the observed experimental results.

## 2. Experimental

### 2.1. Materials

Ammonium cerium(IV) nitrate (98%, $(NH_4)_2Ce(NO_3)_6$), 1,4-benzene dicarboxylic acid (98%, $H_2BDC$), 2,5-pyridine dicarboxylic acid (98%, $H_2PDC$), Zirconium(IV) chloride (99%, $ZrCl_4$), zirconyl(VI) chloride octahydrate (98%, $ZrOCl_2{\cdot}8H_2O$), hafnium(IV) chloride (99%, $HfCl_4$), *n*-butylamine ($CH_3(CH_2)_3NH_2$, ≥99%), formic acid (96%, $CH_2O_2$), and Sodium nitrate ($NaNO_3$, ACS reagent, ≥99.0%) were purchased from Sigma-Aldrich. Acetic acid ($CH_3COOH$, 98.5–100.5%), acetone ($C_3H_6O$, 99%), hydrochloric acid (HCl, 98%), sodium hydroxide (NaOH, 99%), *N*,*N*′-dimethylformamide (DMF, 99 wt%), ethanol ($C_2H_60$, 99.9%), methanol ($CH_3OH$, 99.9%) was supplied by Fine Chemical Co. Ltd and reagent alcohols were purchased from Macron Chemicals. Carbon dioxide ($CO_2$, 99.999%) was purchased from Indura.

### 2.2. Synthesis

All synthetic procedures were performed according to previous literature reports. Zr and Hf-UiO-66 were synthesized following the procedure reported by Farha *et al.*[21] Ce-UiO-66 was synthetized according to the procedure by Lammert *et al.*[32] and Zr-, Hf-, and Ce-UiO-66-PDC were prepared performing the Stock *et al.* procedure.[24] See the ESI† for further information. All products were separated and washed by centrifugation at 8000 rpm for 10 min with the same reaction solvent (2 × 10 mL) and then with ethanol (2 × 10 mL). Finally, they were dried under vacuum at room temperature for three days, except for Hf-UiO-66-PDC, which required over five days to dry.

### 2.3. Characterizations

The textural properties were obtained in a Micromeritics Gemini VII instrument for volumetric nitrogen adsorption–desorption isotherm of nitrogen at −196 °C, using 0.03 g of each sample, which were degassed for 4 hours at 180 °C, under vacuum using a micromeritics VacPrep instrument. The surface area was determined using the Brunauer–Emmett–Teller (BET) theory in the relative pressure range of $0.05 \leq P/P_0 \leq 0.25$.[33] Total pore volume was defined as the single-point pore volume at $P/P_0 = 0.99$. Micropore volume was calculated from the *t*-plot equation, and pore size distribution was obtained by applying the nonlinear density functional theory (NLDFT) equation.[34] ATR-FTIR spectroscopy was achieved on a Shimadzu spectrum two equipment with an ATR accessory. Each spectrum was obtained with 20 accumulations in a wavenumber range of 4000 to 500 $cm^{-1}$ with a 2 $cm^{-1}$ resolution. The powder X-ray diffraction (PXRD) patterns were registered in a Bruker D2 Phaser diffractometer using a Cu Kα radiation ($\beta$ = 1.541840 Å) from a Cu X-ray tube, operated at 30 kV and 10 mA. TGA analysis was performed on a Mettler-Toledo TGA/SDTA851 instrument. In a typical analysis, 3 to 12 mg were

weighed and transferred to an $Al_2O_3$ sample holder. Then, by flowing a mixture of 20 mL $min^{-1}$ of $N_2$, the samples were heated at a rate of 20 °C $min^{-1}$, and data were collected within a temperature range of 25 °C to 900 °C. Potentiometric titrations for M-UiO-66 were performed according to the method reported by Klet *et al.*[35] In this method, 50 mg of each sample was dispersed in approximately 60 mL of $NaNO_3$ 0.1 M and allowed to equilibrate for 18 h. The solution's pH was adjusted to 3 using HCl 0.1 M, and then titrated with standardized NaOH 0.1 M until a pH of 11.

### 2.4. $CO_2$ adsorption capacity and isosteric heat

All $CO_2$ adsorption isotherms were measured in a Micromeritics Gemini VII instrument at 263, 273, and 283 K until 100 kPa in a batch system. The points collected on the adsorption measurement were fitted with the Freundlich–Langmuir equation (eqn (1)),

$$n = \frac{a \cdot (b \cdot p)^c}{1 + (b \cdot p)^c} \quad (1)$$

where $n$ is the amount adsorbed in mmol $g^{-1}$, $p$ is the absolute pressure in kPa, $a$ constant is the maximal loading in mmol $g^{-1}$, $b$ is the affinity constant in $kPa^{-1}$, and $c$ is the heterogeneity exponent. The Langmuir isotherm is based on the model of a monolayer on a solid and is often used to fit type I isotherms on microporous solids with complete pore filling, as it is defined in Brunauer, Deming, Deming and Teller classification (BDDT).[36,37] With the Freundlich–Langmuir fit, the Clausius–Clapeyron equation (eqn (2)) was used to calculate the isosteric heat of adsorption as follows:

$$\frac{dp}{dT} = \frac{\Delta H_{ads}}{T \cdot \Delta V} \quad (2.1)$$

$$Q_{st}(n) = -R \cdot \ln\left(\frac{p_2}{p_1}\right) \frac{T_1 \cdot T_2}{T_2 - T_1} \quad (2.2)$$

when the enthalpy of adsorption $\Delta H_{ads}$ from the eqn (2.1) is a function of the gas uptake ($n$) we can use $Q_{st}$ to refer to the isosteric heat of adsorption. The eqn (2.2) takes this form when three considerations are made: (i) ideal gas behavior of the gas phase, (ii) a negligible molar volume of the liquid-like adsorbed phase, and (iii) a constant value of the enthalpy of adsorption in the measured temperature range, therefore an interval of 20 K have been selected for these purposes, applying a large temperature range ($\Delta T$ > 20 K) will introduce an error no longer negligible.[36] Note that as the pressure increases, the approximations (i) and (ii) begin to induce error, but at the pressure of 100 kPa (the maximum measured pressure) those errors are still negligible.[38] Further details can be found in the ESI.†

### 2.5. Computational details

Due to the large size of extended network structures such as MOFs, the simulations involve high computational cost. One way to address the significant size issue of MOFs is by truncating a periodic structure to a smaller representative fragment that accurately represents the structure of interest.[39] The representative fragment is named "cluster models".[40] This approach has been widely discussed in the literature, with many previous studies. Those studies highlight that even though MOFs are extended network structures, these structures often exhibit highly localized electronic states. In the herein study, the cluster model proposed is based on previous works,[41–43] which consist of a node and ligands acting as linkers. Specifically, the cluster model structure consists of the fragments $[M_6O_4(OH)_4(linker)_3(HCOO)_8]$ (M = Zr(IV), Ce(IV), and Hf(IV); linker = BDC or PDC), see Fig. S1.† This model contains one node $[M_6O_4(OH)_4]^{12-}$, three complete linkers, seven truncated linkers, and considers only a single defect or vacancy. The simulations were conducted using the DFT method, which was implemented in the ADF2023 software package.[44] In these systems, relativistic effects are necessary due to the presence of heavy metals, which can significantly impact the materials' chemical and physical properties. Accounting for relativistic effects is essential for an accurate description of the electronic structure and properties of the chemistry of these systems.[45] Therefore, in the herein simulations, the relativistic effects were incorporated using the zeroth-order regular approximation approach (ZORA).[46] Geometry optimizations were performed at the *meta*-generalized gradient approximation (*meta*-GGA) level of theory using the M06-L exchange–correlation energy functional.[47] The standard Slater-type orbital basis set plus two polarization functions (STO-TZ2P) was selected for all calculations.[48] The interactions between M-UiO-66 with different linkers and $CO_2$ were examined using energy decomposition analysis (EDA) based on the Morokuma–Ziegler scheme.[49,50] Furthermore, to accurately consider the use of dispersion forces in EDA computations, Grimme's D3 dispersion correction incorporated weak interactions between the fragments.[51] To conduct the EDA analysis, the ADF program was employed, using the *meta*-hybrid TPSSH functional[52,53] at the TZ2P/ZORA level of theory, which is a better functional to describe electronic structure and energies of systems. This analysis breaks down the interaction energy ($\Delta E_{Int}$), as shown in eqn (3).

$$\Delta E_{Int} = \Delta E_{Pauli} + \Delta E_{Elec} + \Delta E_{Orb} + \Delta E_{Disp} \quad (3)$$

The repulsive interaction between the occupied orbitals of both fragments is called $\Delta E_{Pauli}$ term.[54] Thsecond term, $\Delta E_{Elec}$, accounts for the classic electrostatic interaction between the two segments.[43] Interactions involving molecular orbitals associated with charge transfer, polarization, and other factors are included in the third term, $\Delta E_{Orb}$.[55] The dispersion contribution are represented by the term $\Delta E_{Disp}$.[56] Additionally, the natural orbital of chemical valence (NOCV) approach proposed by Mitoraj was employed to analyze the orbital contribution.[57] This scheme considers the formation of an interacting system AB (with the wave function $\psi_{AB}$) from its respective fragments. In this scheme, the NOCV defines the charge-flow channels decomposing the overall deformation density $\Delta\rho$. The NOCV are expressed in this equation as adding the pairs of comp-

 

lementary eigenfunctions ($\psi_{-k}$, $\psi_k$) that correspond to the eigenvalues $\nu_k$ and $-\nu_k$. These eigenvalues have the same absolute value but differ in sign:[58]

$$\Delta\rho_{\mathrm{orb}}(r) = \pi r^2(r) = \sum_{k=1}^{\frac{N}{2}} \Delta\rho_k \nu_k \left[-\psi_{-k}{}^2(r) + \psi_k{}^2(r)\right] = \sum_{k=1}^{\frac{N}{2}} \Delta\rho_k(r) \quad (4)$$

The complementary pairs of NOCV define the charge-flow channels between the molecular fragments. When considering pairs of NOCVs ($\psi_{-k}$, $\psi_k$) with identical absolute eigenvalues $|\nu_k|$, an outflow $\Delta\rho_{\mathrm{orb}}$ [outflow($i$)] and inflow $\Delta\rho_{\mathrm{orb}}$ [inflow($i$)] of electron density can be determined within each $\Delta\rho_{\mathrm{orb}}(i)$. By means of eqn (5), it is possible to examine these terms individually, explicitly focusing on the processes of electron density outflow and inflow from a specific fragment.[54,59]

$$\Delta\rho_{\mathrm{orb}}(r) = \sum_{k=1}^{N/2} \left[\Delta\rho_{\mathrm{orb}}^{\mathrm{outflow}}(i) + \Delta\rho_{\mathrm{orb}}^{\mathrm{inflow}}(i)\right] \quad (5)$$

The interaction energies were adjusted using the counterpoise approach due to the presence of the basis set superposition error (BSSE).[60]

## 2.6. Adsorption kinetics

**2.6.1. Apparent kinetic model.** Pseudo-first order, pseudo-second order, and Avrami's kinetic model were applied to determine the $CO_2$ adsorption rate and check if the model changes between the materials. Avrami's kinetic is a fractional model for particle nucleation and has recently been applied to describe adsorption on solid materials.[61] Eqn (6)–(11) show the general and integrated form of the three models.Pseudo-first order

$$\frac{\mathrm{d}q_t}{\mathrm{d}t} = k_1(q_e - q_t) \quad (6)$$

$$q_t = q_e\ (1 - e^{-k_1 t}) \quad (7)$$

Pseudo-second order

$$\frac{\mathrm{d}q_t}{\mathrm{d}t} = k_s(q_e - q_t)^2 \quad (8)$$

$$q_t = \frac{k_s q_e{}^2 t}{1 + q_e k_s t} \quad (9)$$

Avrami's model

$$\frac{\mathrm{d}q_t}{\mathrm{d}t} = k_A^{n_A} t^{(n_A - 1)}(q_e - q_t) \quad (10)$$

$$q_t = q_e\left(1 - e^{-(k_A t)^{n_A}}\right) \quad (11)$$

where $q_t$ is the amount adsorbed (mmol $g^{-1}$) in time $t$, $q_e$ is the amount adsorbed (mmol $g^{-1}$) at equilibrium ($t = \infty$), $k_1$ pseudo-first-order kinetic constant ($min^{-1}$), $k_s$ pseudo-first-order kinetic constant (mmol $g^{-1}$ $min^{-1}$), $k_A$ the Avrami kinetic constant ($min^{-1}$), $n_A$ is the Avrami exponent reflecting mechanism changes that may occur during adsorption and it also represents the dimensionality of the growth of adsorption sites: $n_A = 2$ for one-dimensional growth, $n_A = 3$ for two-dimensional growth, and $n_A = 4$ for three-dimensional growth.[62,63] The points collected on the adsorption measurement were fitted with the eqn (7), (9), and (11) in a nonlinear fit.

**2.6.2. Rate-limiting kinetic model.** Three diffusion models were used to identify the rate-limiting stage for comprehending $CO_2$ adsorption. In solid porous materials, the adsorption mechanism mainly includes five steps: (i) bulk diffusion: $CO_2$ molecules transfer from the bulk phase to the outer surface of the adsorbent; (ii) film diffusion: molecules pass through the gas film around the solid adsorbents, (iii) interparticle diffusion: molecules diffuse from one particle to another, (iv) intraparticle diffusion: molecules diffuse in the pores of the adsorbent (v) surface adsorption: molecules are adsorbed by the active sites. Usually, steps (i) and (v) are faster for an adsorption process, so the adsorption rate is controlled by one of the other steps or a combination of them.[64]

*(a) Boyd's film diffusion model.* This model assumes that the gas film surrounding the adsorbent is the main resistance to the adsorption of the adsorbate. The model is expressed as follows:[62]

$$F = 1 - \frac{6}{\pi^2}\sum_{n=1}^{\infty}\frac{1}{n^2}\exp\left(-n^2 B_t\right) \quad (12)$$

where $F$ is the fractional adsorption capacity at a given time ($F = q_t/q_e$), $B_t$ is a mathematical function of $F$.For

$$F > 0.85, B_t = -0.4977 - \ln(1 - F) \quad (13)$$

For

$$F < 0.85, B_t = \left(\sqrt{\pi} - \sqrt{\pi - \frac{\pi^2 F}{3}}\right)^2 \quad (14)$$

Eqn (12)–(14) can be used to determine whether the rate of $CO_2$ adsorption occurs by film diffusion or an intraparticle diffusion mechanism and to predict the mechanical steps involved in the adsorption process. While the plot of $B_t$ *versus* $t$ indicates that intraparticle diffusion is the rate-limiting step if the curve crosses the linear origin. However, film diffusion or a chemical reaction also significantly impacts the adsorption rate if the plot is nonlinear or does not pass through the origin.[62,64,65]

*(b) Interparticle model.* The model assumes that the interparticle diffusion model is the rate-limiting step; it assumes that the shape of the adsorbent is equivalent to spheres and the diffusivity is constant in spherical coordinate. The expression gives the integrated formula:

$$\frac{q_t}{q_e} = 1 - \frac{6}{\pi^2}\sum_{n=1}^{\infty}\frac{1}{n^2}\exp\left(-\frac{n^2\pi^2 D_c t}{r_p{}^2}\right) \quad (15)$$

Eqn (15) can be used to obtain the diffusion time constant $t_D = D_c/r_p{}^2$ ($s^{-1}$) and $q_t/q_e$ have already been explained. When $q_t/q_e > 70\%$ eqn (15) can be simplified as:

$$1 - \frac{q_t}{q_e} \approx \frac{6}{\pi^2}\exp\left(-\frac{n^2\pi^2 D_c t}{r_p{}^2}\right) \quad (16)$$

Then, if interparticle diffusion is the rate-limiting step, a plot of $\ln(1 - q_t/q_e)$ against $t$ should be linear with a slope $-D_c/r_p^2$ and the intercept $\ln(6/\pi^2)$. Otherwise, the adsorption is controlled by other steps.[62,65,66]

*(c) Intraparticle model.* Weber–Morris proposed the intraparticle model based on the Fick's second law.[67] This model can be used to identify consecutive stages of mass transfer during the adsorption model. The adsorption capacity is linear with the square root of time according to the expression:

$$q_t = k_{id} t^{1/2} + C \quad (17)$$

where $k_{id}$ is the intraparticle diffusion rate constant (mmol $g^{-1}$ $min^{-1/2}$), and $C$ refers to the thickness of the boundary layer (mmol $g^{-1}$).

According to this model, the plot $q_t$ *versus* $t^{1/2}$ should give a straight line if diffusion plays a role in the rate of adsorption, and this line should pass through the origin if intraparticle diffusion is the sole rate-controlling step. Multi-linearity can be observed when different steps are involved in the adsorption mechanism, where the linear portion having the lowest slope corresponds to the rate-controlling step.[62,64,65]

# 3. Results and discussion

## 3.1. Structural and textural properties of MOFs

The FT-IR analysis presented in Fig. S2† indicates that the main differences between the structures are related to the bands located at 555, 660, and 740 $cm^{-1}$ for the M-UiO-66. These bands correspond to the vibrations of the $\mu_3$-OH, $\mu_3$-O, and M–OH bonds present in the SBU of each MOFs, except for Ce-UiO-66 and Ce-UiO-66-PDC, where the $\mu_3$-O bond is not present.[32,68] On the other hand, the Ce–O, Hf–O, and Zr–O bonds in UiO-66 are assigned to the band observed in the 550–743 $cm^{-1}$ range. The C=C vibration mode of terephthalic acid ligands was attributed to the vibrations at 1506–1589 $cm^{-1}$. The C–O stretching mode was assigned to the strong bands at 1393 $cm^{-1}$, whereas the characteristic band at 1664 $cm^{-1}$ was attributable to the vibration mode of C=O. On the other hand, MOFs synthesized with PDC (M-UiO-66-PDC) exhibit the C=C vibrational mode of the disubstituted pyridine group with vibrations in the region between 1400–1594 $cm^{-1}$. Meanwhile, three weak signals were observed between 1025 and 1200 $cm^{-1}$ associated with the C–N bond, which is characteristic of pyridine.

The crystallinity of the synthesized MOFs was evaluated using PXRD for all materials. It can be observed in Fig. S3a and Table S1† that all MOFs are isoreticular and with a fcc structure. The two characteristic peaks at 5 degrees are observed in all samples,[16] where the first peak is more intense than the second one. The only exception is Ce-UiO-PDC which shows the same intensity for both peaks, which could be due to the sample treatment issue as it was challenging to work with this powder with large static (which tends to stick over every surface). Those two initial peaks are used as reference for all the forthcoming peaks. Thus, Zr and Ce MOFs have the same peaks and intensity proportion with no displacement. In case of the Hf MOFs there are some extra peaks at 10 and 26 degrees when the linker is changed to PDC. Table S1† shows that Hf-UiO-66-PDC has an 80.3% of crystallinity, while the other MOFs have >95% of crystallinity, probably the water content on the synthesis process affects the crystals growth and morphology of this MOF. Those extra peaks get displaced and decrease in intensity maintaining similar percentage of crystallinity when the material is activated at 180 °C for 4 hours (see Fig. S3b†), suggesting the re-accommodation of some collapsed unit cells in a minor proportion.

Generally, changing the linker does not affect the crystallinity or the structure, whereas changing the metal center produces small displacements on the crystal structure attributed to the change of the metal radius.

The surface area was determined using the BET equation to measure the available surface area of the synthesized materials. All synthesized materials showed type I isotherms according to BDDT classification (Fig. S4†),[37] except for Ce-UiO-66-PDC and Hf-UiO-66-PDC, which showed hysteresis, a type IV isotherm which is related to a contribution of mesoporous behavior. It is possibly that the activation process generated some wide pores by collapsing some of the unit cells. In case of Hf-UiO-66-PDC the entire structure collapse has been reported.[24] Nonetheless, according to what has been observed in Fig. S3b,† it is postulated that the loss of crystallinity causes the formation of some mesopores without a collapse of the structure (see Fig. S5†).

On both Zr(IV) MOFs large surface areas with no significant difference can be seen, with respect to similar reports found in the literature (Table S2†).[24,32,69,70] A trend of surface area decrease occurs with Ce(IV) and Hf(IV) MOFs. There is an increase in the surface area when the MOF is more defective.[25,71] This described behavior correlates with Ce and Hf synthesized with PDC linker having fewer defects than their BDC analogs (see Table 1). While the decrease in the surface area for these MOFs could be due to the formation of some mesopores on Ce-UiO-66-PDC and Hf-UiO-66-PDC.

For the BDC MOFs, Zr and Hf have similar surface areas, whereas Ce shows a decrease to 925 $m^2$ $g^{-1}$. In general, these MOFs have identical surface areas near the previously reported. The observed differences could be due to the defects of our materials and the difference in atomic radius ($Hf^{4+}$ = 71 pm < $Zr^{4+}$ = 72 pm < $Ce^{4+}$ = 87 nm). The radii trend Hf < Zr < Ce can explain the generation of bulkier clusters for Ce(IV), reducing the pore volume and the surface area. Thus, the surface areas measured correlate well with this trend. Thus, there is a competition on the influence over the surface area between the atomic radius and the defect sites in the structure. Previous reports associate an increase ~200 $m^2$ $g^{-1}$ in the surface area (Zr-UiO-66) with the loss of one missing linker.[71] In case of PDC-MOFs, the surface areas show dependence on defects in the structures, where Zr-UiO-66-PDC is the most defective of the PDC-MOFs, then Ce-UiO-66-PDC and finally Hf-UiO-66-PDC (Table 1).

 

Table 1 Calculated number of defects, BET area, and micropore volume ($V_0$) of M-UiO-66 and M-UiO-66-PDC

| Material | Missing linker | Molecular formula | MW (g mol$^{-1}$) | $S_{BET}$ (m$^2$ g$^{-1}$) | $V_0$ (cm$^3$ g$^{-1}$) |
|---|---|---|---|---|---|
| Zr-UiO-66 | 0.9[a] | $Zr_6O_4(OH)_4(C_8H_4O_4)_{5.15}[(H_2O)(OH)]_{1.7}$ | 1584 | 1188 | 0.46 |
| Zr-UiO-66-PDC | 1.9[b] | $Zr_6O_4(OH)_4(PDC)_{4.1}$ | 1356 | 1083 | 0.42 |
| Ce-UiO-66 | 1.9[a] | $Ce_6O_4(OH)_4(C_8H_4O_4)_{4.15}[(H_2O)(OH)]_{3.7}$ | 1783 | 925 | 0.42 |
| Ce-UiO-66-PDC | 1.3[b] | $Ce_6O_4(OH)_4(PDC)_{4.7}$ | 1748 | 626 | 0.30 |
| Hf-UiO-66 | 1.1[a] | $Hf_6O_4(OH)_4(C_8H_4O_4)_{4.95}[(H_2O)(OH)]_{2.1}$ | 2085 | 1196 | 0.42 |
| Hf-UiO-66-PDC | 0.5[b] | $Hf_6O_4(OH)_4(PDC)_{5.5}$ | 2111 | 509 | 0.16 |

[a] Missing linker determined by potentiometric titration. [b] Missing linker determined by thermogravimetric analysis. See ESI† for further information.

### 3.2. $CO_2$ adsorption capacity

$CO_2$ adsorption isotherms at 263, 273, and 283 K were measured to estimate the adsorption capacities of the synthesized MOFs, calculate the isosteric heat of adsorption, and evaluate the influence of the metal center and the linker. All measurements (Fig. 1) show, as predicted, that the amount adsorbed decreases as the temperature increases due to the diminution of interactions with a kinetic energy rise of the gas. On Zr and Hf MOFs an increase in $CO_2$ uptake is observed when the linker is changed to PDC, even though the surface area of both compounds decreases from BDC to PDC. This observation supports the importance of replacing one carbon with a nitrogen atom in the aromatic linker, producing an increase of the material with $CO_2$ attractive interactions. The affinity of polar nitrogen with the quadrupolar moment of $CO_2$ is probably the dominant interaction on the adsorption. Another evidence of the interaction increase can be seen in the isotherm shapes (Fig. 1). As observed in Fig. 1, all the herein studied MOFs have better uptakes at low pressures (from 10 to 40 kPa) with PDC linker, while the isotherms behavior is nearly linear with BDC linker for the $CO_2$ adsorptions at those pressures. High uptakes at low pressures can be directly related to an increase in intermolecular interactions.[36]

The results show that the most suitable materials for $CO_2$ adsorption are Ce MOFs and Zr-UiO-66-PDC with adsorptions greater than 4 mmol g$^{-1}$. Those three MOFs have a more significant number of defects, Zr-UiO-66-PDC being the material with the larger number of defects. As discussed, if the number of defects turns larger the surface area gets also larger, creating more sites to interact. Those interaction sites correspond for example to $\mu_3$-OH. Also, the diversity in the structure (due to the large defect number) favors the interaction with $CO_2$ as the metallic center is more available to interact. On the other hand, in the case of Hf MOFs another interesting situation is observed, where there is better $CO_2$ adsorption on Hf-UiO-66-PDC, which is less defective than Hf-UiO-66. Thus, the nitrogen of the aromatic cycle on PDC MOFs also increases $CO_2$ adsorption. Finally, the effect of the metal center must also be considered (not only absence of linker), which can be tricky to analyze due to the large defect variety. In general, the $CO_2$ adsorption performance trend by metal centers is Ce > Zr > Hf. As shown in the FTIR characterizations, Ce MOFs do not possess the $\mu_3$-O group, whereas the $\mu_3$-OH is more intense. This intensity difference might be due to the water affinity of Cerium causing a fully hydroxylated cluster. Thus, the positively $\mu_3$-OH charged hydrogen site can interact with the negatively charged $CO_2$ oxygen, behavior that has been reported before.[25] This behavior has shown to increase the adsorption capacities of Ce MOFs.

Both Ce MOFs (BDC and PDC) adsorbed a high and similar amount of $CO_2$, but there was an unexpected decrease in the maximum uptake when the linker is changed to PDC. Despite this exception to the detected trend, it is observed that there is an increase in intermolecular interactions when the linker is changed, supported by isothermal shapes. Thus, the decrease observed for Ce derivatives could be due to surface area and pore size limitations as Ce MOFs have minor surface areas if compared with their analogs, with an even larger diminution when PDC is the linker. Fig. 2 shows the intrinsic adsorption of $CO_2$ which is obtained from the quotient between the $CO_2$ adsorption at 263 K and 95 kPa with the respective surface area and the number of defects of the material. As observed the intrinsic adsorption of Ce-UiO-66-PDC is greater than Ce-UiO-66, showing that when surface area and defects are normalized the effect of the PDC linker increase de adsorption capacities of Ce MOFs.

According to the intrinsic adsorption on Fig. 2, the $CO_2$ adsorption capacities of Zr MOFs are the same, showing that apparently the linker does not affect the adsorption capacities of Zr MOFs. However, on PDC MOFs the intrinsic adsorption trend is Hf > Ce > Zr, which suggest that raising the oxophilicity character (which follows the same trend[72]) of the metal center in presence of the pyridine group there are also raising of the electronic interaction of $CO_2$ over the metallic cluster of the material and a shortening of the bond length between $CO_2$ and $\mu_3$-O according to the theoretical analysis discussed below.

### 3.3. Computational analysis

The optimized geometries of the ground state ($S_0$) using the cluster model matched the values predicted by previous theoretical calculations for extended UiO-66 and UiO-66-PDC structures and the experimentally reported data,[73,74] indicating a good description of the system. A list with selected interatomic distances (see ESI†) can be found in Table S6.† These data show that the average [M–O ($\mu_3$-OH)], [M–O ($\mu_3$-O)], and [M–O ($COO^-$)] bond lengths show a good correlation with previous reports at the M06-L/TZ2P/ZORA theoretical level for M-UiO-66 and M-UiO-66-PDC. Based on these results, we proceeded with simulations of the interacting systems M-UiO-66

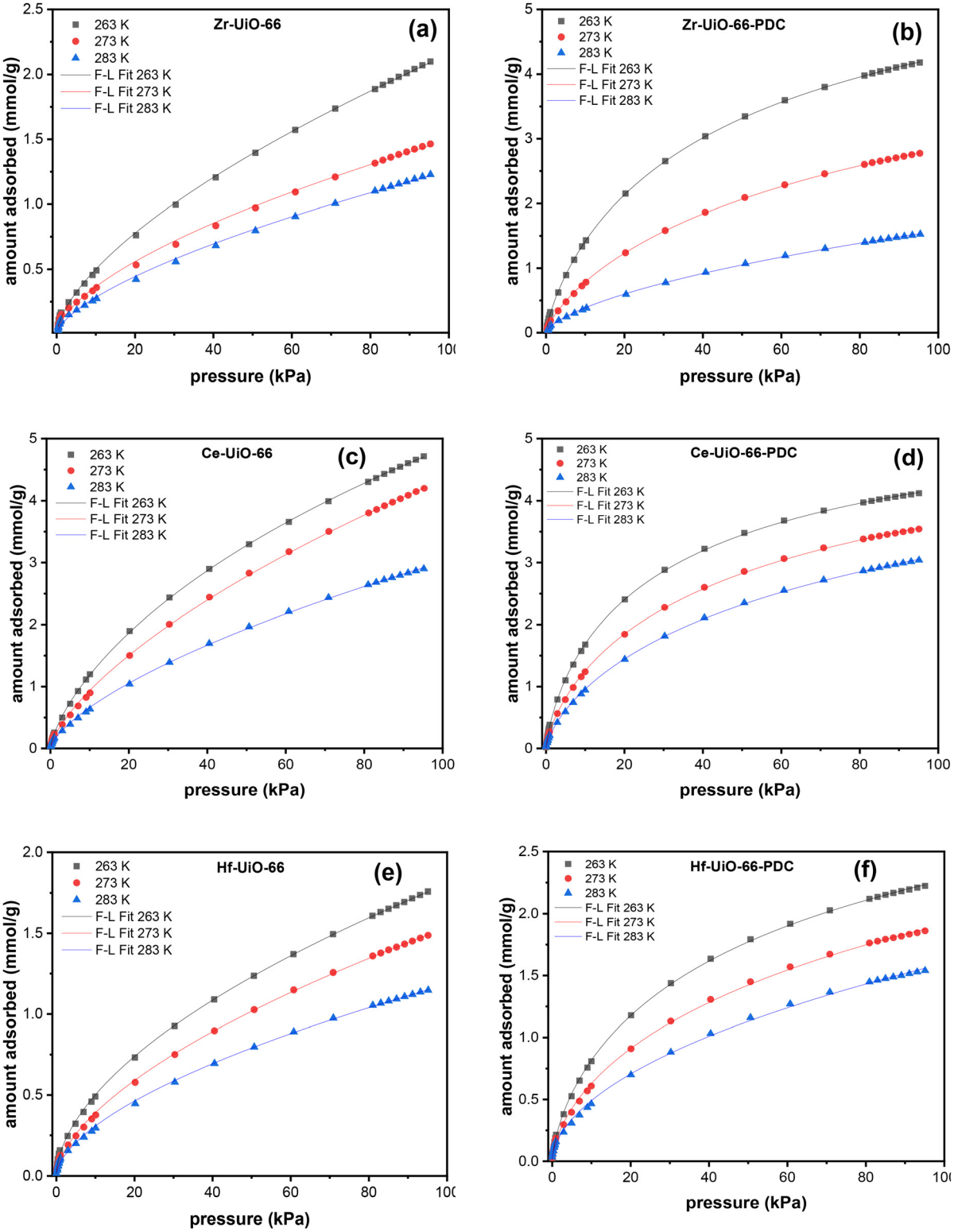


**Fig. 1** $CO_2$ adsorption isotherms at 263 K (black), 273 K (red) and 283 K (blue) of Zr-UiO-66 (a), Zr-UiO-66-PDC (b), Ce-UiO-66 (c), Ce-UiO-66-PDC (d), Hf-UiO-66 (e) and Hf-UiO-66-PDC (f).

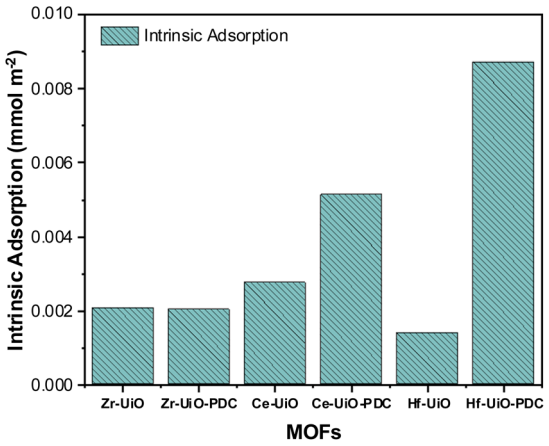


**Fig. 2** Intrinsic adsorption of M-UiO-66 (M = Zr(IV), Ce(IV), Hf(IV)) with BDC linker or PDC linker.

and M-UiO-66-PDC and $CO_2$, using a cluster model. In these simulations, differences in weak and medium strength acid sites were observed in M-UiO-66 with different linkers, corresponding to $M^{n+}$ and $\mu_3$-OH, created from the missing linkers. Thus, in our cluster model, we considered a single defect as well as a starting structure of the M-UiO-66 and M-UiO-66-PDC/$CO_2$ where the $CO_2$ interacts with the defect site, see Fig. S11.† The optimized structures of the M-UiO-66 and M-UiO-66-PDC with $CO_2$ $S_0$ electronic states are displayed in Table S7.† In all systems, it is possible to observe that the geometry of M-UiO-66 and M-UiO-66-PDC/$CO_2$ systems converged to the $CO_2$ interacting mainly with the defect sites. For M-UiO-66 and M-UiO-66-PDC/$CO_2$, the $CO_2$ is in a position closer to the metal center and M–$\mu_3$-O–H of the defect site. The calculated length between $CO_2$ and the metal center (M⋯$CO_2$) is in average 3.08 Å for all systems. While the average distance for –$\mu_3$-OH⋯$CO_2$ for the M-UiO-66 and M-UiO-66-PDC/$CO_2$ systems is 3.17 Å and 3.20 Å for the distance –$\mu_3$-O⋯$CO_2$, see Table S8.† The EDA Analysis scheme and the NOCV approach were used to gain a deeper understanding of the M-UiO-66 and M-UiO-66-PDC/$CO_2$ interactions. These analyses provide insights into the nature and strength of the different interaction types, such as electrostatic, polarization, and dispersion forces. As shown in Table S9,† the interaction energies suggest that the interaction between M-UiO-66 and M-UiO-66-PDC with $CO_2$ does not exceed −8.46 kcal mol$^{-1}$, which indicates a predominance of long-range interactions.

These results show that the electrostatic component has the most crucial role in stabilizing energy, with more than 40% contribution in all systems. For M-UiO-66/$CO_2$ the orbital term shows a slightly larger percentual contribution than the dispersive component of the total attractive energies. In contrast, for M-UiO-66-PDC/$CO_2$ systems, the orbital term has a slightly smaller percentual contribution than the dispersive term. The role of the interaction between the oxygen lone pairs (of the $CO_2$) with the metal center or $\mu_3$-O–H groups in these systems could be significant if the electrostatic and orbital contribution to the total stabilization energy are considered. This assumption is confirmed with the NOCV deformation density channels analysis, as discussed below. Thus, NOCV analysis indicated that the main deformation density channel ($\Delta\rho_1$) is originated from the lone electron pair of $CO_2$ electron donation (red color (outflow)) to the metal center (blue color (charge accumulation)) in the defect sites of M-UiO-66 and M-UiO-66-PDC. While other contributions to the deformation density channels $\Delta\rho_2$ display a donor–acceptor interaction that involves the (O⋯H) interaction from the oxygen atom $CO_2$ molecule lone electron pair and the MOF -$\mu_3$-OH hydrogen atom, see Fig. S12 and S13.†

By means of DFT calculations it can be supported that the Hf-UiO-66 has the larges $CO_2$ adsorption, due to the small observed interaction energy, which supports the easy release of the adsorbed gas.

### 3.4. Kinetics of gas phase $CO_2$ adsorption on MOFs

The effect of temperature on the $CO_2$ adsorption curves for Zr-UiO-66 is illustrated in Fig. 3, which shows similar behavior as all the herein studied MOFs (see Fig. S17†). As shown in this figure, the $CO_2$ adsorption times and dynamic adsorption capacities significantly decreased with increasing adsorption temperature due to the exothermic nature of the adsorption process.[75–78] The adsorption curves have been fitted with pseudo-first order, pseudo-second order and Avrami's kinetic models to see if the model varies between the materials or by temperature effect. The fitting results are shown in Fig. S15–S17,† while the kinetic model parameters are shown in Tables S10 and S11.† The Avrami's fractional-order model fitted to all experimental curves with values of $R^2 > 0.99$, being independent of the analyzed MOF or analyzed temperatures, while pseudo-first order and pseudo-second order overestimated or underestimated the $CO_2$ uptake at different adsorption steps (reaching $R^2$ value of not greater than 0.98). Thus, Avrami's equation is considered the most accurate approach to describe the $CO_2$ adsorption. This model has been previously used to explain complex kinetic processes that involve more than one

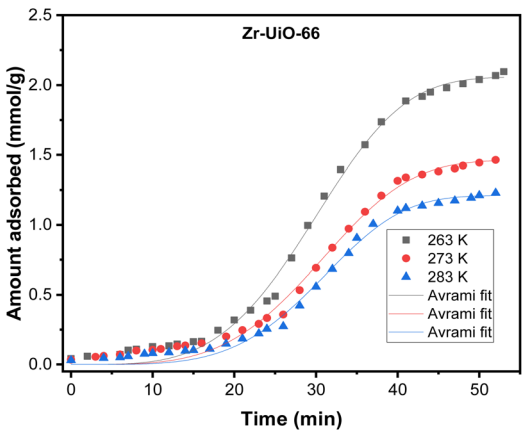


**Fig. 3** Effect of temperature on curves of $CO_2$ adsorption onto Zr-UiO-66 against time.

adsorption mechanism,[62,79] as shown by the herein studied materials.

In the Avrami's equation (see Table S10†), the $K_{AV}$ can be associated with the rate of adsorption, the $n_{AV}$ is associated with changes on the mechanism of adsorption that may occur and the dimensionality of the growth of adsorption sites, and the $q_e$ is related with the amount of $CO_2$ adsorbed by the material at the pressure of 95 kPa. The $q_e$ values for each material show a similar value as the last point obtained in the $CO_2$ adsorption isotherms, which indicates the good of fitness of the equation, but does not give much information about the maximum capacities of the materials because it has been seen that $CO_2$ adsorption of MOFs can still increase at pressures more than 40 bar.[80,81] As the Avrami's exponent ($n_{Av}$) accounts for possible mechanism changes that may occur during the adsorption process, which is the case of our materials with values in the range of 2.8–4.5. Depending on the material, the values vary with temperature up to a maximum adsorption value at 273 or 283 K. For Zr-UiO-66-PDC, Ce-UiO-66 and Hf-UiO-66-PDC the maximum value is reached at 273 K. In contrast, the rest of the MOFs show its maximum at 283 K. This observation is consistent with the theoretical analysis, as the $CO_2$ interacts were characterized to be located overactive sites generated by the defects (missing linker). All MOFs have identical characteristics of crystal structure, mechanism, and rate of adsorption, as shown by the adsorption rate constant's ($K_{Av}$). This constant has no significant variation between the material and temperatures and the Avrami's exponents. At 273 K for Zr-UiO-66-PDC, the adsorption rate constant generates that the curve (Fig. S17†) is slightly displaced towards the 263 K curve.

In order to elucidate the actual rate-controlling and the mechanism of diffusion associated with the $CO_2$ adsorption on the synthesized materials, film diffusion, interparticle diffusion and intraparticle diffusion model have been analyzed. Thus, Fig. S18† shows the film diffusion plot of Boyds parameter ($B_t$) against time for each material under different temperatures. The Boyd plot produces usually for diffusion systems a straight line, whereas if the systems show as limiting step the diffusion or chemical reaction, it shows a nonlinear behavior or a linear behavior that does not pass through the axis origin. In this case, all curves exhibited a nonlinear behavior at the three analyzed temperatures. Therefore, we can support the fact that film diffusion as one of the factors that influence the $CO_2$ adsorption rate.

Interparticle diffusion is the rate-limiting step if the plot of $\ln(1 - q_t/q_e)$ against time is linear with a slope $-D_c/{r_p}^2$ and the intercept $\ln(6/\pi^2)$. In Fig. S19† is shown the interparticle diffusion plot for each material at different temperatures (the corresponding calculated parameters are listed in Table S12†). At the analyzed temperatures, a nonlinear behavior plots are observed for all materials. Besides, the intercepts are displaced from the value $\ln(6/\pi^2)$. These two previously shown results disregard the interparticle diffusion as the rate-limiting step.

Fig. S20† shows the intraparticle diffusion plot of $q_t$ *versus* $t^{1/2}$ for each material at different temperatures. As can be observed all curves exhibit multi-linearity, indicating that there are different steps involved in the adsorption mechanism. It is expected that intraparticle diffusion will be a limiting step due to the abundant number micropores present in the materials. Finally, the third linear segment, zone C, is attributed to the final equilibrium step, where the materials are near saturation.

The above results show how the materials adjust to the Avrami's model, used to explain complex kinetic processes like the recently analyzed, where the $CO_2$ adsorption rate is mainly controlled by pore filling in the first stage of adsorption, and then intraparticle diffusion resistance is the $CO_2$ adsorption rate controlling until the adsorption reaches an equilibrium close to saturation. These results are very close to the Yang *et al.*[65] ones, showing that probably most MOFs have complex and similar adsorption mechanisms.

### 3.5. Isosteric heat of adsorption

The isosteric heat of adsorption is a measure of the energy required for the adsorption of a gas over a surface. This value was first calculated for MOFs using the Clausius–Clapeyron equation in 2005 for $[M_3(bpdc)_3bpy]4DMF{\cdot}H_2O$ (M = Zn or Co),[82] since then, the isosteric heat have been calculated for a wide variety of materials.

For $CO_2$ adsorption, MOFs (such as Hf-UiO-66-$F_4$,[30] Zr-UiO-67-BBS[31] and Mg-MOF-74[83]) are capable of adsorbing this gas in the range of 1.2 to 8.0 mmol $g^{-1}$ at pressures and temperature near to 273 K and 1 bar (see Table S13† for further information), while isosteric heats of adsorption are in the range of 20 to 50 kJ $mol^{-1}$. The herein studied MOFs are also in this range of $CO_2$ adsorption and isosteric heat, except for Zr-UiO-66-PDC, which has unexpectedly high released heat. It is essential to calculate the isosteric heat to apply the materials for its right applications, such as separation of gas mixtures,[19,62,84] gas storage,[85] adsorption cooling, heat pump, and desalination.[86,87] As all the mentioned applications require favorable isosteric heat for their process.

Thus, the isosteric heat of $CO_2$ adsorption was calculated (Fig. 4) to evaluate the different possibilities of applications of the herein studied MOFs. It is important to mention that the fit from eqn (1) fails at low pressures (see Fig. S9†), so the modeled isosteric heat at lower gas uptakes show the largest error. We thus attributed the low $Q_{st}$ for Hf-UiO-66-PDC to this error.

Zr-UiO-66-PDC has an unusual large isosteric heat curve compared to the other studied MOFs, indicating a stronger surface affinity for the $CO_2$ molecule. Furthermore, a chemisorption process has been discarded due to a negligible adsorption difference after five adsorption/desorption cycles, showing more than 97% of physisorption of $CO_2$ (see Fig. S10†).

There is an increment in the released heat when the linker is changed to PDC (Fig. 4 and S22†). In this sense, the change on the nature in the linker induces an increase interaction with the $CO_2$ molecule, as the pyridine linker possess an electron lone pair. Furthermore, an increment in the isosteric heat has been reported when defects are more frequent.[88] This cor-

 

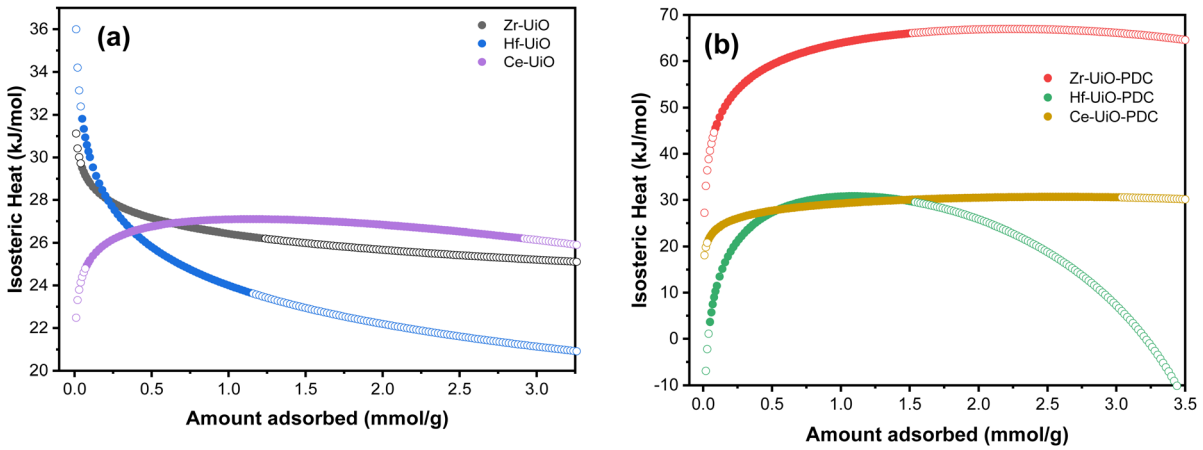


**Fig. 4** The isosteric heat of adsorption ($Q_{st}$) in a function of the $CO_2$ amount adsorbed of M-UiO-66 (M = Zr(IV), Hf(IV), Ce(IV)) with (a) BDC linker or (b) PDC linker. Filled symbols represent the amount adsorbed of each material at 283 K and open symbols represent the modeled $Q_{st}$.

relates with the fact that Zr-UiO-66-PDC has the largest released heat and the most significant number of defects. A similar situation is observed in the case of BDC MOFs, where Ce-UiO-66 is the most defective MOF and has the largest measured isosteric heat.

It can be observed that, at low uptakes, the isosteric heat increases or decreases with the pore filling, depending on the material. Zr and Hf-UiO-66 have decreasing isosteric heat with increasing material loading. On the other hand, the remaining MOFs increase their isosteric heat with increasing material loading. The usual discussion focuses on the heterogeneity or homogeneity of the studied materials, where heterogeneous materials have few high-energy sites that become saturated at the initial of the adsorption. Then, at high coverage, the energy is mainly dispersed. While in homogeneous material, the energy just increases with the adsorption due to the adsorbate–adsorbate repulsions.[89–91] However, the herein reported materials are isoreticular, thus the possess the same topology and adsorption sites. Thus, there is no cause for Zr and Hf-UiO-66 to have high energy sites, whereas the other studied materials show another trend, thus the explanation for the trends seems to follow another behavior. Pendleton *et al.*[92] introduced the assumption of the linear summation of three distinct heats to give the isosteric heat of adsorption: condensation heat due to fluid–fluid ($q_{f-f}$) interactions, non-specific interaction heat due to fluid–solid ($q_{f-s}$) as dispersion forces, and specific interaction heat due to fluid–high energy sites ($q_{f-HES}$).[92] Base on that proposed separation scheme for the isosteric heat, the high energy sites are not present for the herein studied MOFs. The remaining two interactions left (condensation heat ($q_{f-f}$) and non-specific interaction heat ($q_{f-s}$)) are the ones contributing to the difference in the isosteric heats. On the $q_{f-f}$ heat it is expected that, at near to zero pore filling, the gas molecules would be isolated on the adsorber, and there would be no fluid–fluid interactions contributing to the overall isosteric heat. Thus, with increasing pore filling, these interactions also increase its contribution to the heat to a value equivalent to the adsorptive latent heat of condensation. Otherwise, the $q_{f-s}$ heat is the interaction of the material with the gas, which gradually decreases with pore-filling due to the occupation of the surface with the adsorptive molecules. Applying those approximations to a slit-shaped micropore, the gas molecules would be adsorbed on pores of width like the fluid molecule's kinetic diameter and subsequently on slightly larger pores with decreased interaction energy. As a result, $q_{f-f}$ contributes an ascendent heat with increasing pore filling, while $q_{f-s}$ contributes a descendent curve to the overall isosteric heat.[92]

As previously mentioned, the calculated isosteric heat of the herein studied materials for Zr and Hf-UiO-66 have the $q_{f-s}$ heat as the predominant contribution, while the remaining studied materials have the $q_{f-f}$ heat predominating. In case of the BDC MOFs, Ce-UiO-66 has a different trend than Zr and Hf-UiO-66, which can be attributed to the number of defects of Ce-UiO-66 which is almost twice of the Zr and Hf-UiO-66 defects. The large number of present defects in case of Ce-UiO-66 generates a difference on the adsorption sites causing proximity between the adsorbed $CO_2$ molecules which can be related to a larger $q_{f-f}$ heat contribution. In the case of the PDC MOFs, they all have the same trend of $q_{f-f}$ heat predominance (same as Ce-UiO-66), and the $CO_2$ adsorption for these materials is better than their BDC analogs, except for Ce-MOFs which shows significant $CO_2$ adsorption for both materials. The high saturation levels of Ce-UiO-66 and Ce-UiO-66-PDC with $CO_2$ could be the reason for the dominance of $q_{f-f}$ heat in the overall isosteric heat for these materials. Likewise, Zr and Hf-UiO-66 have a distinguished distinctive contribution of $q_{f-s}$ heat because there is a higher interaction between the surface of these materials and the adsorbed gas molecules.

Finally, the three main parameters that influence the $CO_2$ adsorption could be correlated, as shown in Fig. 5. As observed, there is a clear dependency between the defects and/or available surface area with the $CO_2$ adsorbed amount.

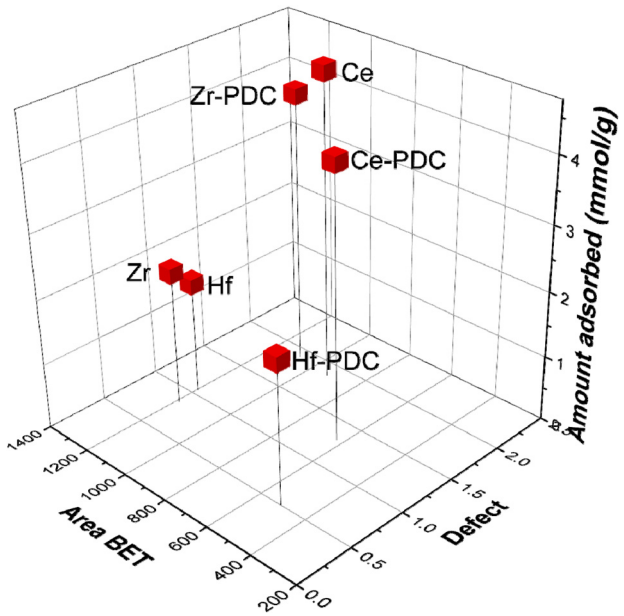


**Fig. 5** Correlation between the BET surface area, $CO_2$ adsorbed amount, and defect sites.

## 3. Conclusions

In this study, six UiO-MOFs synthesized varying the metal center between Zr(IV), Ce(IV), or Hf(IV) and the linker between BDC or PDC showed some differences in the structural and textural properties. It is essential to highlight the absence of the $\mu_3$-O bond on Ce-UiO-66 and Ce-UiO-66-PDC the high crystallinity of all synthesized MOFs, and the different surface areas of the material, which generated significant changes in the adsorption capacities, where the number of defects also played a substantial role, together with the surface areas of the materials, the intrinsic properties of the metal centers and the linkers. The lone pair of the PDC nitrogen linker improved the $CO_2$ adsorption capacities of the materials (not depending on the metal center) due to the interaction with the quadrupolar moment of the $CO_2$. Ce-UiO-66-PDC showed a reduced $CO_2$ adsorption compared with Ce-UiO-66, but this was attributed to a surface area limitation and not a reduction adsorbent–adsorbate interaction. Ce and Zr-UiO-66-PDC MOFs showed the best $CO_2$ adsorption capacities with amounts greater than 4 mmol $g^{-1}$. The high capacities of adsorption were attributed to the high number of defects and the surface area contributing together, and the Ce MOFs case attributed that the absence of the $\mu_3$-O bond and the increased amount of $\mu_3$-OH bonds created more favorable interactions with $CO_2$.

By means of DFT calculations using the EDA-NOCV scheme it was possible to study the nature of the MOF–$CO_2$ interactions, showing that the $CO_2$ preferently interacts with the defect sites, supporting the experimentally observed results.

The kinetics of adsorption studies showed an adjustment to the Avrami's fractional-order kinetic model independent of the studied material or temperature. The Avrami's model is used to explain complex kinetic processes like the analyzed applying the rate-limiting kinetic models of Boyd's film diffusion, interparticle and intraparticle, concluding that the $CO_2$ adsorption rate on the synthesized MOFs is mainly controlled by diffusion on the first stage. Then, intraparticle diffusion resistance controls the $CO_2$ adsorption rate until the adsorption reaches an equilibrium close to saturation.

Finally, the calculation of the isosteric heat of adsorption confirmed an increment in the $CO_2$ interaction with the PDC linker and it was observed an increment of the $Q_{st}$ with defects, where both PDC linker and number of defects explained the unexpectedly high released heat of Zr-UiO-66-PDC.

## Conflicts of interest

There are no conflicts to declare.

## Acknowledgements

FONDECYT 1241917, 1231194, ANID/FONDAP/ 1523A0006, ACT210057, Programa de Iniciativa científica Milenio ANID-NCN2021_090 and beca Doctorado ANID 21211190. ANID Postdoctoral 3230141.

## References

1 A. Arenillas, K. M. Smith, T. C. Drage and C. E. Snape, in *Fuel*, 2005, vol. 84, pp. 2204–2210.
2 C. H. Yu, C. H. Huang and C. S. Tan, *Aerosol Air Qual. Res.*, 2012, **12**, 745–769.
3 L. Wang, M. Yao, X. Hu, G. Hu, J. Lu, M. Luo and M. Fan, *Appl. Surf. Sci.*, 2015, **324**, 286–292.
4 N. Gargiulo, F. Pepe and D. Caputo, *J. Nanosci. Nanotechnol.*, 2014, **14**, 1811–1822.
5 M. G. Plaza, C. Pevida, A. Arenillas, F. Rubiera and J. J. Pis, *Fuel*, 2007, **86**, 2204–2212.
6 M. S. Shafeeyan, W. M. A. W. Daud, A. Houshmand and A. Shamiri, *J. Anal. Appl. Pyrolysis*, 2010, **89**, 143–151.
7 S. Cavenati, C. A. Grande and A. E. Rodrigues, *J. Chem. Eng. Data*, 2004, **49**, 1095–1101.
8 C. Chen, D. W. Park and W. S. Ahn, *Appl. Surf. Sci.*, 2014, **292**, 63–67.
9 A. Sayari and Y. Belmabkhout, *J. Am. Chem. Soc.*, 2010, **132**, 6312–6314.
10 S. Cho, H. R. Yu, K. D. Kim, K. B. Yi and Y. S. Lee, *Chem. Eng. J.*, 2012, **211–212**, 89–96.
11 J. An and N. L. Rosi, *J. Am. Chem. Soc.*, 2010, **132**, 5578–5579.
12 K. O. Kirlikovali, S. L. Hanna, F. A. Son and O. K. Farha, *ACS Nanosci. Au*, 2023, **3**(1), 37–45.
13 G. E. Cmarik, M. Kim, S. M. Cohen and K. S. Walton, *Langmuir*, 2012, **28**, 15606–15613.

14 P. Serra-Crespo, E. V. Ramos-Fernandez, J. Gascon and F. Kapteijn, *Chem. Mater.*, 2011, **23**, 2565–2572.
15 A. R. Millward and O. M. Yaghi, *J. Am. Chem. Soc.*, 2005, **127**, 17998–17999.
16 J. H. Cavka, S. Jakobsen, U. Olsbye, N. Guillou, C. Lamberti, S. Bordiga and K. P. Lillerud, *J. Am. Chem. Soc.*, 2008, **130**, 13850–13851.
17 T. Islamoglu, D. Ray, P. Li, M. B. Majewski, I. Akpinar, X. Zhang, C. J. Cramer, L. Gagliardi and O. K. Farha, *Inorg. Chem.*, 2018, **57**, 13246–13251.
18 Q. Yang, A. D. Wiersum, P. L. Llewellyn, V. Guillerm, C. Serre and G. Maurin, *Chem. Commun.*, 2011, **47**, 9603–9605.
19 Y. Jiang, C. Liu, J. Caro and A. Huang, *Microporous Mesoporous Mater.*, 2019, **274**, 203–211.
20 S. J. Garibay and S. M. Cohen, *Chem. Commun.*, 2010, **46**, 7700–7702.
21 M. J. Katz, Z. J. Brown, Y. J. Colón, P. W. Siu, K. A. Scheidt, R. Q. Snurr, J. T. Hupp and O. K. Farha, *Chem. Commun.*, 2013, **49**, 9449–9451.
22 A. Huang, L. Wan and J. Caro, *Mater. Res. Bull.*, 2018, **98**, 308–313.
23 Y. Goji, R. Abdullahi, Y. Garba, J. Japhet, D. Kitgak and K. Dangkat, *Nigerian Journal of Materials Science and Engineering*, **2021**, 1–13.
24 S. Waitschat, D. Fröhlich, H. Reinsch, H. Terraschke, K. A. Lomachenko, C. Lamberti, H. Kummer, T. Helling, M. Baumgartner, S. Henninger and N. Stock, *Dalton Trans.*, 2018, **47**, 1062–1070.
25 H. Wu, Y. S. Chua, V. Krungleviciute, M. Tyagi, P. Chen, T. Yildirim and W. Zhou, *J. Am. Chem. Soc.*, 2013, **135**, 10525–10532.
26 J. W. M. Osterrieth, J. Rampersad, D. Madden, N. Rampal, L. Skoric, B. Connolly, M. D. Allendorf, V. Stavila, J. L. Snider, R. Ameloot, J. Marreiros, C. Ania, D. Azevedo, E. Vilarrasa-Garcia, B. F. Santos, X. H. Bu, Z. Chang, H. Bunzen, N. R. Champness, S. L. Griffin, B. Chen, R. B. Lin, B. Coasne, S. Cohen, J. C. Moreton, Y. J. Colón, L. Chen, R. Clowes, F. X. Coudert, Y. Cui, B. Hou, D. M. D'Alessandro, P. W. Doheny, M. Dincă, C. Sun, C. Doonan, M. T. Huxley, J. D. Evans, P. Falcaro, R. Ricco, O. Farha, K. B. Idrees, T. Islamoglu, P. Feng, H. Yang, R. S. Forgan, D. Bara, S. Furukawa, E. Sanchez, J. Gascon, S. Telalović, S. K. Ghosh, S. Mukherjee, M. R. Hill, M. M. Sadiq, P. Horcajada, P. Salcedo-Abraira, K. Kaneko, R. Kukobat, J. Kenvin, S. Keskin, S. Kitagawa, K. ichi Otake, R. P. Lively, S. J. A. DeWitt, P. Llewellyn, B. V. Lotsch, S. T. Emmerling, A. M. Pütz, C. Martí-Gastaldo, N. M. Padial, J. García-Martínez, N. Linares, D. Maspoch, J. A. Suárez del Pino, P. Moghadam, R. Oktavian, R. E. Morris, P. S. Wheatley, J. Navarro, C. Petit, D. Danaci, M. J. Rosseinsky, A. P. Katsoulidis, M. Schröder, X. Han, S. Yang, C. Serre, G. Mouchaham, D. S. Sholl, R. Thyagarajan, D. Siderius, R. Q. Snurr, R. B. Goncalves, S. Telfer, S. J. Lee, V. P. Ting, J. L. Rowlandson, T. Uemura, T. Iiyuka, M. A. van der Veen, D. Rega, V. Van Speybroeck, S. M. J. Rogge, A. Lamaire, K. S. Walton, L. W. Bingel, S. Wuttke, J. Andreo, O. Yaghi, B. Zhang, C. T. Yavuz, T. S. Nguyen, F. Zamora, C. Montoro, H. Zhou, A. Kirchon and D. Fairen-Jimenez, *Adv. Mater.*, 2022, **34**(27), 2201502.
27 S. Biswas and P. Van Der Voort, *Eur. J. Inorg. Chem.*, 2013, 2154–2160.
28 Y. Huang, W. Qin, Z. Li and Y. Li, *Dalton Trans.*, 2012, **41**, 9283–9285.
29 R. Dalapati, B. Sakthivel, A. Dhakshinamoorthy, A. Buragohain, A. Bhunia, C. Janiak and S. Biswas, *CrystEngComm*, 2016, **18**, 7855–7864.
30 Z. Hu, A. Nalaparaju, Y. Peng, J. Jiang and D. Zhao, *Inorg. Chem.*, 2016, **55**, 1134–1141.
31 P. Xydias, I. Spanopoulos, E. Klontzas, G. E. Froudakis and P. N. Trikalitis, *Inorg. Chem.*, 2014, **53**, 679–681.
32 M. Lammert, M. T. Wharmby, S. Smolders, B. Bueken, A. Lieb, K. A. Lomachenko, D. De Vos and N. Stock, *Chem. Commun.*, 2015, **51**, 12578–12581.
33 S. Brunauer, P. H. Emmett and E. Teller, *Adsorption of Gases in Multimolecular Layers*, 1938.
34 G. Kupgan, T. P. Liyana-Arachchi and C. M. Colina, *Langmuir*, 2017, **33**, 11138–11145.
35 R. C. Klet, Y. Liu, T. C. Wang, J. T. Hupp and O. K. Farha, *J. Mater. Chem. A*, 2016, **4**, 1479–1485.
36 A. Nuhnen and C. Janiak, *Dalton Trans.*, 2020, **49**, 10295–10307.
37 S. Brunauer, L. S. Deming, W. Edwards Deming and E. Teller, *J. Am. Chem. Soc.*, 2002, **62**, 1723–1732.
38 H. Pan, J. A. Ritter and P. B. Balbuena, in *Thermodynamic Functions of Gases*, ed. F. Din, Prentice Hall, 1985, vol. 81.
39 Y. Hidalgo-Rosa, M. A. Treto-Suárez, E. Schott, X. Zarate and D. Páez-Hernández, *J. Comput. Chem.*, 2020, **41**, 1956–1964.
40 J. L. Mancuso, A. M. Mroz, K. N. Le and C. H. Hendon, *Chem. Rev.*, 2020, **120**, 8641–8715.
41 X. P. Wu, L. Gagliardi and D. G. Truhlar, *J. Am. Chem. Soc.*, 2018, **140**, 7904–7912.
42 E. Camu, C. Pazo, D. Becerra, Y. Hidalgo-Rosa, D. Paez-Hernandez, X. Zarate, E. Schott and N. Escalona, *New J. Chem.*, 2020, **44**, 14865–14871.
43 C. Pazo-Carballo, E. Blanco, E. Camu, A. Leiva, Y. Hidalgo-Rosa, X. Zarate, A. B. Dongil, E. Schott and N. Escalona, *ACS Appl. Nano Mater.*, 2023, **6**(7), 5422–5433.
44 G. te Velde, F. M. Bickelhaupt, E. J. Baerends, C. Fonseca Guerra, S. J. A. van Gisbergen, J. G. Snijders and T. Ziegler, *J. Comput. Chem.*, 2001, **22**, 931–967.
45 M. Atanasov, D. Aravena, E. Suturina, E. Bill, D. Maganas and F. Neese, *Coord. Chem. Rev.*, 2015, **289–290**, 177–214.
46 E. Van Lenthe, E. J. Baerends, J. G. Snijders, E. Van Lenthe, E. J. Baerends and J. G. Snijders, *J. Chem. Phys.*, 1993, **99.6**, 4597–4610.
47 Y. Zhao and D. G. Truhlar, *J. Chem. Phys.*, 2006, **125**(19), 194101.
48 E. Van Lenthe and E. J. Baerends, *J. Comput. Chem.*, 2003, **24**, 1142–1156.

49 K. Kitaura and K. Morokuma, *Int. J. Quantum Chem.*, 1976, **10**, 325–340.
50 T. Study and H. T. Method, *Society*, 1979, **18**, 1755–1759.
51 S. Grimme, *Wiley Interdiscip. Rev.: Comput. Mol. Sci.*, 2011, **1**, 211–228.
52 J. Tao, J. P. Perdew, V. N. Staroverov and G. E. Scuseria, *Phys. Rev. Lett.*, 2003, **91**, 3–6.
53 V. N. Staroverov, G. E. Scuseria, J. Tao and J. P. Perdew, *J. Chem. Phys.*, 2003, **119**, 12129–12137.
54 F. Sagan and M. P. Mitoraj, *J. Phys. Chem. A*, 2019, **123**, 4616–4622.
55 M. P. Mitoraj, A. Michalak and T. Ziegler, *J. Chem. Theory Comput.*, 2009, **5**, 962–975.
56 S. Grimme, J. Antony, S. Ehrlich and H. Krieg, *J. Chem. Phys.*, 2010, **132**, 5585.
57 M. P. Mitoraj, *J. Phys. Chem. A*, 2011, **115**, 14708–14716.
58 M. P. Mitoraj, A. Michalak and T. Ziegler, *Organometallics*, 2009, **28**, 3727–3733.
59 K. Devi, S. M. N. V. T. Gorantla and K. C. Mondal, *J. Comput. Chem.*, 2022, **43**, 757–777.
60 S. F. Boys and F. Bernardi, *Mol. Phys.*, 1970, **19**, 553–566.
61 M. Songolzadeh, M. Soleimani and M. Takht Ravanchi, *J. Nat. Gas Sci. Eng.*, 2015, **27**, 831–841.
62 N. Álvarez-Gutiérrez, M. V. Gil, F. Rubiera and C. Pevida, *Chem. Eng. J.*, 2017, **307**, 249–257.
63 J. B. Benedict and P. Coppens, *J. Phys. Chem. A*, 2009, **113**, 3116–3120.
64 S. Loganathan, M. Tikmani, S. Edubilli, A. Mishra and A. K. Ghoshal, *Chem. Eng. J.*, 2014, **256**, 1–8.
65 F. Yang, X. Zhu, J. Wu, R. Wang and T. Ge, *Powder Technol.*, 2022, **399**, 117090.
66 G. Song, X. Zhu, R. Chen, Q. Liao, Y. D. Ding and L. Chen, *Chem. Eng. J.*, 2016, **283**, 175–183.
67 J. C. Morris and W. J. Weber, *Adv. Water Pollut. Res.*, 1964, 231–266.
68 L. Valenzano, B. Civalleri, S. Chavan, S. Bordiga, M. H. Nilsen, S. Jakobsen, K. P. Lillerud and C. Lamberti, *Chem. Mater.*, 2011, **23**, 1700–1718.
69 G. C. Shearer, S. Chavan, J. Ethiraj, J. G. Vitillo, S. Svelle, U. Olsbye, C. Lamberti, S. Bordiga and K. P. Lillerud, *Chem. Mater.*, 2014, **26**, 4068–4071.
70 M. J. Cliffe, W. Wan, X. Zou, P. A. Chater, A. K. Kleppe, M. G. Tucker, H. Wilhelm, N. P. Funnell, F. X. Coudert and A. L. Goodwin, *Nat. Commun.*, 2014, **5**, 4176.
71 M. R. DeStefano, T. Islamoglu, S. J. Garibay, J. T. Hupp and O. K. Farha, *Chem. Mater.*, 2017, **29**, 1357–1361.
72 V. R. Bakuru, S. R. Churipard, S. P. Maradur and S. B. Kalidindi, *Dalton Trans.*, 2019, **48**, 843–847.
73 S. Huang, D. G. Truhlar, A. Tang, X. He, H. Yin, Y. Li and Y. Zhang, *J. Phys. Chem. C*, 2021, **125**, 9679–9687.
74 S. Øien, D. Wragg, H. Reinsch, S. Svelle, S. Bordiga, C. Lamberti and K. P. Lillerud, *Cryst. Growth Des.*, 2014, **14**, 5370–5372.
75 Y. Zhao, Y. Shen, L. Bai and S. Ni, *Appl. Surf. Sci.*, 2012, **261**, 708–716.
76 R. Zafari, F. G. Mendonça, R. Tom Baker and C. Fauteux-Lefebvre, *Sep. Purif. Technol.*, 2023, **308**, 1383–5866.
77 A. C. Lua and T. Yang, *Chem. Eng. J.*, 2009, **155**, 175–183.
78 M. Auta and B. H. Hameed, *Chem. Eng. J.*, 2014, **253**, 350–355.
79 E. C. N. Lopes, F. S. C. Dos Anjos, E. F. S. Vieira and A. R. Cestari, *J. Colloid Interface Sci.*, 2003, **263**, 542–547.
80 W. Kukulka, K. Cendrowski, B. Michalkiewicz and E. Mijowska, *RSC Adv.*, 2019, **9**, 18527–18537.
81 W. Liang, C. J. Coghlan, F. Ragon, M. Rubio-Martinez, D. M. D'Alessandro and R. Babarao, *Dalton Trans.*, 2016, **45**, 4496–4500.
82 J. Y. Lee, L. Pan, S. P. Kelly, J. Jagiello, T. J. Emge and J. Li, *Adv. Mater.*, 2005, **17**, 2703–2706.
83 S. R. Caskey, A. G. Wong-Foy and A. J. Matzger, *J. Am. Chem. Soc.*, 2008, **130**, 10870–10871.
84 S. Sircar, R. Mohr, C. Ristic and M. B. Rao, *J. Phys. Chem. B*, 1999, **103**, 6539–6546.
85 L. Lei, Y. Cheng, C. Chen, M. Kosari, Z. Jiang and C. He, *J. Colloid Interface Sci.*, 2022, **612**, 132–145.
86 B. Han and A. Chakraborty, *Int. J. Heat Mass Transfer*, 2022, **186**, 122473.
87 B. Han and A. Chakraborty, *Energy Convers. Manage.*, 2020, **213**, 112825.
88 P. Ghosh, Y. J. Colón and R. Q. Snurr, *Chem. Commun.*, 2014, **50**, 11329–11331.
89 S. G. Musa, Z. M. Aljunid Merican and A. Haruna, *J. Solid State Chem.*, 2022, **314**, 123363.
90 A. Chakraborty, B. B. Saha, S. Koyama and K. C. Ng, *Appl. Phys. Lett.*, 2006, **89**(17), 171901.
91 J. A. Dunne, M. Rao, S. Sircar, R. J. Gorte and A. L. Myers, *Langmuir*, 1996, **12**, 5896–5904.
92 S. H. Madani, S. Sedghi, M. J. Biggs and P. Pendleton, *ChemPhysChem*, 2015, **16**, 3797–3805.